Progress in Oceanography 156 (2017) 61–77

Contents lists available at ScienceDirect

Progress in Oceanography

journal homepage: www.elsevier.com/locate/pocean

Analysis of longer period variation of the Kuroshio Current intrusion into the Luzon Strait using rectified wavelet power spectra

Yaochu Yuan [a,*], Chenghao Yang [a], Yu-heng Tseng [b], Xiao-Hua Zhu [a], Huiqun Wang [a], Hong Chen [a]

[a] State Key Laboratory of Satellite Ocean Environment Dynamics, Second Institute of Oceanography, State Oceanic Administration, Hangzhou 310012, PR China
[b] Institute of Oceanography, National Taiwan University, Taipei 10650, Taiwan

ARTICLE INFO

Article history:
Received 28 September 2016
Received in revised form 15 March 2017
Accepted 4 April 2017
Available online 2 June 2017

Keywords:
Luzon Strait currents
ADCP and TD measurements
Rectified wavelet power spectra
Dominant period of 112 d
Kuroshio meandering
Interaction of eddies with Kuroshio

ABSTRACT

Longer period variation of the Kuroshio into the Luzon Strait (LS) was identified using acoustic Doppler current profiler (ADCP) observations as well as pressure and temperature time series data recorded by two TDs (manufactured by the RBR Ltd.) at mooring station N2 (20°40.441′N, 120°38.324′E). The ADCP was deployed at depths of 50–300 m between July 7, 2009 and April 10, 2011, and the TDs at around 340 and 365 m between July 9, 2009 and July 9, 2011. Observations provide strong evidence of longer period variation of the Kuroshio into the LS using the Vector rotary spectra (VRS) and Rectified wavelet power spectra analysis (RWPSA). RWPSA of the observations allowed the identification of two types of dominant periods. The first type, with the strongest power spectral density (PSD), had a dominant period of 112 d and was found throughout the upper 300 m. For example, the maximum PSD for western and northern velocity components time series were 3800 and 3550 at 50 m, respectively. The maximum power spectral density decrease with deeper depths, i.e., the depth dependence of maximum PSD. The 112 d period was also identified in the pressure and temperature time series data, at 340 m and 365 m. Combined RWPSA with VRS and mechanism analysis, it is clear that the occurrence of the most dominant period of 112 d in the upper 300 m is related to the clockwise meandering of the Kuroshio into the LS, which is caused by westward propagating stronger anticyclonic eddies from the interior ocean due to the interaction of Rossby eddies with the Kuroshio. The second type of dominant period, for example a 40 d period, is related to the anticlockwise meandering of the Kuroshio. The final dominant period of 14 d coincides with the fortnightly spring-neap tidal period.

1. Introduction

The interaction between the Kuroshio current and the South China Sea (SCS) through the Luzon Strait (LS) has attracted significant attention in recent decades, as reviewed in Nan et al. (2015). Observational and numerical results have indicated that the northward Kuroshio current, located east of the LS, extends downward to about 700 m, and a westward intrusion from the Kuroshio occurs at depths of above 400 m in the LS (Yuan et al., 2007, 2008, 2009a, 2012a, 2012b, 2014a; Tseng et al., 2012). Many studies have focused on the westward intrusion of the Kuroshio into the SCS through the LS. Mechanisms driving the Kuroshio intrusion into the SCS are mainly related to seasonal variation of the East Asia monsoon (e. g., Metzger and Hurlburt, 1996; Qu, 2000; Fang et al., 2003, 2009; Cai et al., 2005, 2012; Liu et al., 2008; Qu et al., 2009). The westward intrusion is commonly stronger during winter than during summer. However, the El Niño Southern Oscillation (ENSO) also has a critical impact on the strength of the intrusion at the interannual time scale (e. g., Qu et al., 2004, 2009; Liu et al., 2008; Chen et al., 2010; Yuan et al., 2014a, 2014b). The intrusion tends to be stronger (weaker) during El Niño (La Niña) years, and this is one of the key processes conveying climate signals from the Pacific into the SCS. The Kuroshio intrusion may also affect internal wave generation in the LS (Du et al., 2008; Park and Farmer, 2013). However, to the best of our knowledge, there has been no observational or numerical study of longer period variations in the Kuroshio intrusion into the LS to date.

In the LS, most previous current measurement studies have analyzed short period variation (less than one month). For example, moored Long Ranger acoustic Doppler current profiler (ADCP) observations were made at station M1 (20°49′47″N, 120°48′37″E) from March to April 2002, and dominant periods were calculated using vector rotary spectra (VRS) (Yuan et al., 2009b). Yuan et al. (2009b) showed a dominant period of 14 d, namely the fortnightly spring-neap tidal period, at observed depths of 200 m and 800 m.

* Corresponding author.
E-mail addresses: yuanyc6@163.com, yuanyc2@sio.org.cn (Y. Yuan).

http://dx.doi.org/10.1016/j.pocean.2017.04.013
0079-6611/

Based on ADCP current measurements at mooring station M2 (20°59.961′N, 120°30.332′E) from April to Sept, 2008, Liao et al. (2011) also identified a dominant 14 d period in the upper 450 m layer. Additionally, based on mooring observations at M3 (20°03.828′N, 120°36.818′E) (see Fig. 1), Liao et al. (2012) suggested that the smooth variance with a fortnightly spring-neap tidal generated cycle is indicative of only astronomical forcing. However, the observational periods were too short to comprehensively cover the full spectrum of currents in the LS. To study low frequency variability of currents in the LS, continuous long time series observation is needed.

Based on observations from the World Ocean Circulation Experiment PCM-1 moored current meter array in the East Taiwan Channel at 24.5°N from September 19, 1994, to May 27, 1996 combined with TOPEX/Poseidon altimetry data, three limited frequency bands centered near periods of 100 days, 40 days, and 18 days were found (Yang et al., 1999, 2001; Zhang et al., 2001; Lee et al., 2001). On the 100-day timescale, Zhang et al. (2001) pointed that the Kuroshio transport entering the East China Sea is strongly related to meandering of the Kuroshio, which in turn is caused by westward propagating anticyclonic eddies from the interior ocean. Lee et al. (2001) also showed that the dominant current and transport variability occurred on 100-day timescales is caused by warm mesoscale eddys merging with the Kuroshio south of the array causing offshore meandering and flow splitting around the Ryukyu Islands.

In terms of analytical approach, power spectrum analysis of standard time series can be very useful in deriving the dominant periods of physical variables (e.g., velocity vectors, temperature, and pressure). Fourier power spectrum analysis (e.g., Welch, 1967) is the most popular approach for single time series and has been widely applied, with rotary spectra modifications for velocity vectors (Chen and Ma, 1991). However, these approaches are limited to stationary time series, while change in the oceanic environment is commonly non-stationary at different time scales, which complicates interpretation of Fourier power spectra. Wavelet analysis is considered superior to Fourier analysis because it unfolds a time series in both frequency and time domains (Torrence and Compo, 1998), it requires no assumption of stationarity, and can determine not only the dominant modes of variability in frequency but also how those modes vary over time (Torrence and Compo, 1998; Tzeng et al., 2012). However, standard wavelet power spectra can be greatly distorted or biased in favor of low frequencies and large scales (Liu et al., 2007, hereafter LLW07). Consequently, standard wavelet analysis of a time series composed of sinusoidal waves with the same amplitude but different frequencies cannot exactly replicate the spectral peaks, resulting in lower (or higher) peaks for high frequency (or low frequency) waves. This problem can be corrected using the rectified wavelet power spectra analysis (RWPSA) proposed in LLW07. RWPSA divides the spectrum by the scales so that spectral peaks of the same magnitude are similar in size (LLW07). LLW07 further suggested a physically consistent definition of energy for the wavelet power spectrum, based on the square of the transformation coefficient divided by its associated scale. The adjusted wavelet power spectrum results in a substantial improvement in the spectral estimate, allowing for comparison of spectral peaks across scales.

The present study has four objectives. The first is to document the time-varying velocity of currents above the 300 m level at mooring station N2 (20°40.441′N, 120°38.324′E) from July 2009 to March 2011, and the pressure and temperature time series data recorded by two TDs from July 9, 2009 to July 9, 2011 (Fig. 1). This provides a unique and valuable dataset because of the long period of observation. The second objective is to analyze the primary longer period data using vector rotary spectra (VRS) for the time series of subtidal current velocity vectors at different depths. The third objective is to analyze longer period variations of the Kuroshio into the LS using RWPSA. The last objective is to make comparison between the VRS analysis and RWPSA and to investigate causes of the dominant periods.

2. Data sources and characteristics of the Kuroshio intrusion into the LS

Mooring station N2 was deployed in the LS on July 7, 2009, and retrieved on September 20, 2011 (see Fig. 1). An acoustic Doppler current profiler (ADCP) with a maximum observational range of about 600 m was installed at the nominal depth of 315 m. Sensor depths actually ranged between 315 and 520 m (i.e., shallower

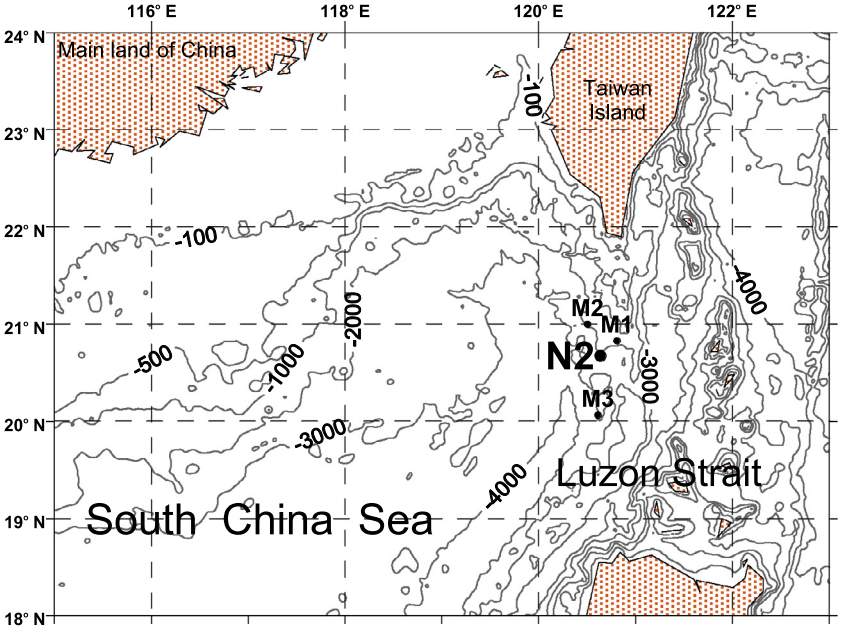

Fig. 1. Location of mooring station N2, M1, M2 and M3 and bottom topography of the Luzon Strait and adjacent areas.

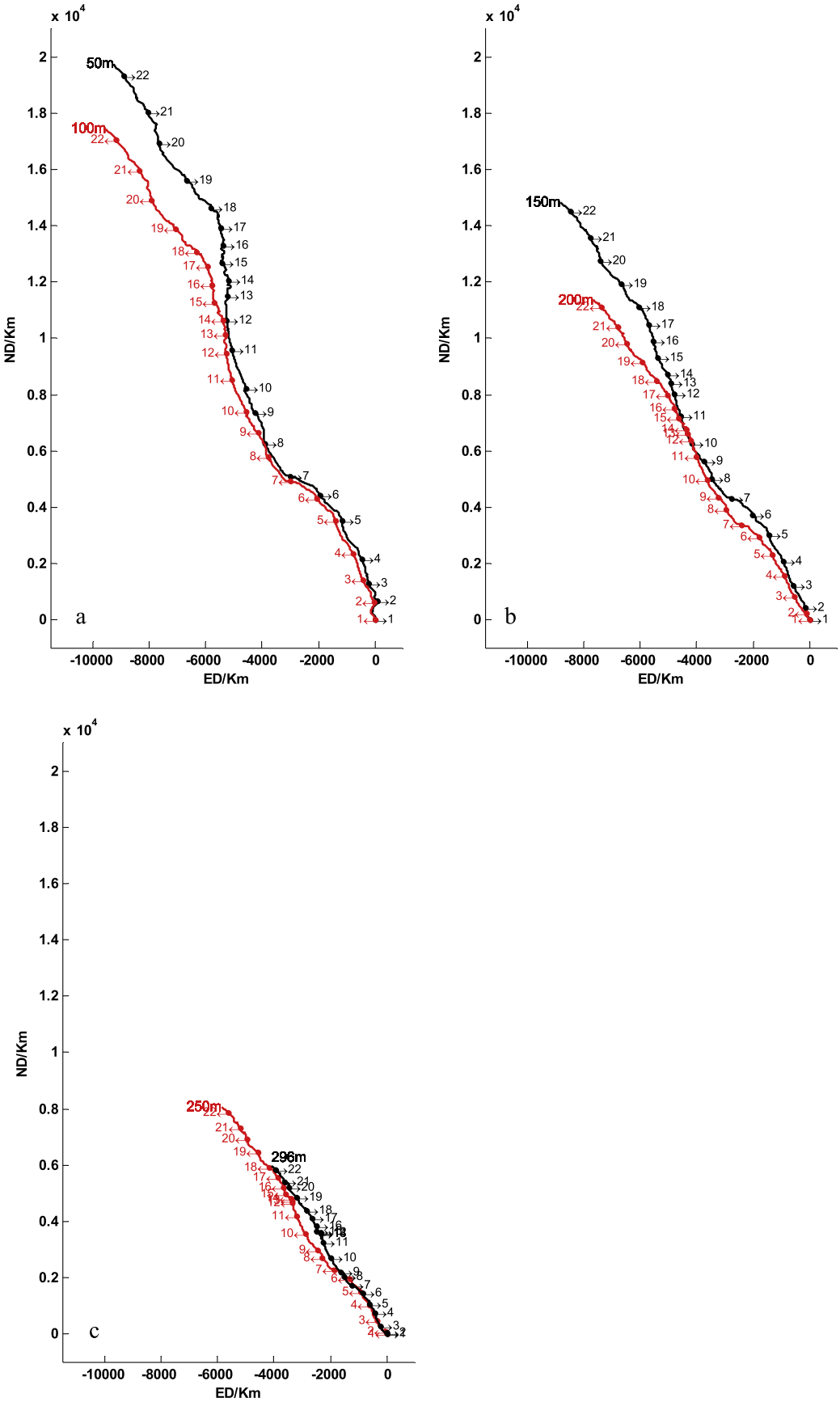

Fig. 2. Progressive vector diagrams of observed daily subtidal currents with the semi-diurnal and diurnal tidal signal removed using a 40 h Chebyshev Ⅱ low pass filter. Currents measured at (a) 50 m and 100 m, (b) 150 m and 200 m, (c) 250 m and 296 m by mooring station N2, from July 7th, 2009 to April 2011. The numbers mark the time of first data of every month from July 7, 2009, till April 10, 2011; namely, 1 is July 7, 207, 2 is August 1, 2009, and 22 is April 1, 2011.(ED and ND denote eastern distance and northern distance, respectively), from Yuan et al. (2014b).

than the sensor's maximum range), due to water flow resistance and drag force exerted on the mooring line. The ADCP collected valid data at depths of 50–300 m, with a 30 min sampling interval, from July 7, 2009 to April 10, 2011.

In order to construct subtidal currents, data was first processed with a 48 h Chebyshev Type II digital low pass filter based on the Welch method (Welch, 1967) to remove periods of less than 48 h. Temperature and pressure time series data were recorded by two TDs (manufactured by RBR Ltd.), fixed to mooring line about 25 m and 50 m below the ADCP, respectively. The TDs (hereafter TD-340 m and TD-365 m) recorded temperature and pressure every minute over almost the entire deployment time (approximately two consecutive years from July 9, 2009 to July 9, 2011). The accuracy of TD temperature was ±0.002 °C, with a drift of less than 0.002 °C/a. Since the results of TD-365 m were consistent with TD-340 m, only representative data from TD-340 m are reported in this paper.

Fig. 2 shows progressive vector diagrams of observed daily subtidal currents at different depths (i.e., semi-diurnal and diurnal tidal signals are removed). The Kuroshio flows generally northwestward above 300 m at the N2 mooring station. Four important characteristics of the Kuroshio are observed in the dataset: (1) The Kuroshio makes successively clockwise and counterclockwise meanders at different scales, as Fig. 2 showed; (2) The strongest intrusion occurs in winter, as indicated in Metzger and Hurlburt (1996) and Yuan et al. (2014b); (3) The strength of the Kuroshio decreases with increasing depth; (4) The average orientation of the Kuroshio changes gradually from NNW to NW with increasing depth.

Yuan et al. (2014b, 2015) discussed seasonal and interannual variability of the Kuroshio intrusion during the same observational period as this study. In terms of seasonal variability, the strongest intrusion occurred in winter (Dec., Jan., and Feb.), with successively weaker currents in spring (Mar., Apr., and May), autumn (Sep., Oct., and Nov.) and summer (Jun., Jul., and Aug.). Furthermore, a summer Kuroshio intrusion through the LS was observed for the first time in 2009, and confirmed by a diagnostic model; this resulted from weaker upstream Kuroshio transport in summer 2009 (period of El Niño initiation) (Yuan et al., 2014a).

3. Analysis of vector rotary spectra (VRS) for the subtidal current time series

In this section, dominant long periods are analyzed using VRS (Chen and Ma, 1991; Yuan et al., 2009b) for the time series of subtidal current velocity vectors at different depths. If we define the following

$$W_m(f) = vS_{x,m}(f)[\eta(f)]^{-1} \tag{3.1}$$

where m is the number of sample series, v is the degree of freedom, $S_{x,m}$ is the smoothed spectra for the sample series,, $\eta(f)$ refers to the expression (10.6.14) of Chen and Ma (1991), and f is the corresponding frequency, $f > 0$ denotes counterclockwise rotary and $f < 0$ denotes clockwise rotary, we can derive the following significance test using a significance level α:

$$W_m(f) > \chi_v^2(1-\alpha) \tag{3.2}$$

If this inequality holds, we can determine the spectral peak is significant. Values for $\chi_v^2(1-\alpha)$ may be obtained from the ordinary mathematical handbook for χ_v^2. For $\alpha = 0.1$ and the degree of freedom $\nu = 4$, $\chi_v^2(1-\alpha) = 7.779$. Fig. 3 shows the corresponding vector rotary low frequency spectral peaks passing the significance test at the depths from 50 m to 296 m, including both clockwise (f < 0, right panel) and counterclockwise (f > 0, left panel) rotary spectra components. From red noise significance tests, the periods 227.5 d and 85.3 d are not prominent spectral peaks in Fig. 3.

Comparing the long period spectral peaks of current velocity vectors in Fig. 3 for both clockwise (f < 0, right panel) and counterclockwise (f > 0, left panel) rotary spectra components, the dominant spectral peaks can be summarized as follows:

(1) Two dominant spectral peaks relative to the tidal signal. One is the fortnightly spring-neap tidal period (14–15 d), with clockwise ($f < 0$) and anticlockwise ($f > 0$) rotary spectra components, and the other is the solid Earth tide (28 d period, 2 × 2 weeks), which mainly occurred in the clockwise rotary spectra component and only occurred at 296 m level for anticlockwise rotary spectra component.
(2) The clockwise rotary spectra component ($f < 0$) showed the dominant current periods of 113.8, 46–49, 19, 16, and 8 d occurred above the 300 m level.
(3) Anticlockwise rotary spectra component ($f > 0$) showed the dominant periods of 8 d, 19 d, 24–26 d and 36–38 d occurred above the 300 m level.

From the above, it is clear that (1) the dominant current periods of 113.8 d only occurred in the clockwise rotary (meandering); (2) the dominant periods of 8 d and 19 d occurred in both the clockwise and anticlockwise rotary spectra components; (3) the dominant periods of 24–26 d and 36–38 d only occurred in the anticlockwise rotary spectra component; (4) the dominant periods of 46–49 d only occurred in the clockwise rotary spectra component. Causes of the dominant periods are addressed in the next section.

4. Analysis of long period variations for the Kuroshio intrusion into the LS using rectified wavelet power spectra analysis

4.1. Rectified wavelet power spectra analysis (RWPSA)

As mentioned in the introduction, RWPSA can effectively rectify distorted wavelet spectra (LLW07). In this section, RWPSA is used to estimate the dominant periods and investigate their causes. The method is briefly described as follows.

Suppose the wavelet basis (Meyer, 1992) is

$$\psi_n^j(t) = 2^{j/2}\psi(2^j t - n), \tag{4.1}$$

where t is real over Re, j and n are the scale level integer and time location, respectively, $\{\psi_n^j(t)\}$ is the normalized mother wavelet that forms a complete orthonormal set with respect to j and n in the function space, L_2, i. e., a space containing square integrable functions over the definition domain (e.g., Meyer, 1992; Liang and Anderson, 2007). Square integrable functions are considered over some finite domain D. Without loss of generality, let D be [0, 1] and introduce another wavelet basis $\tilde{\psi}_n^j(t)$ for the function space over [0, 1], modified from $\{\psi_n^j(t)\}$ in Eq. (4.1) (see detailed derivation in Liang and Anderson, 2007). Liang and Anderson (2007) proved that the new basis $\tilde{\psi}_n^j(t)$ also forms a complete orthonormal system in L_2 [0, 1]. LLW07 adopted the new orthonormal scaling basis $\tilde{\psi}_n^j(t)$, $t \in [0, 1]$. If we have a time series $f(t)$, $t \in [0, 1]$, the transform pair of $f(t)$ can be derived based on the modified wavelet basis $\tilde{\psi}_n^j(t)$ as follows.

$$\hat{f}_n^j = \int_0^1 f(t)\tilde{\psi}_n^j(t)dt,\ j \geqslant 0,\ n = 0, 1, \ldots, 2^j - 1 \tag{4.2}$$

$$f(t) = f_0 + \sum_{j=0}^{\infty}\sum_{n=0}^{2j-1}\hat{f}_n^j\tilde{\psi}_n^j(t) \tag{4.3}$$

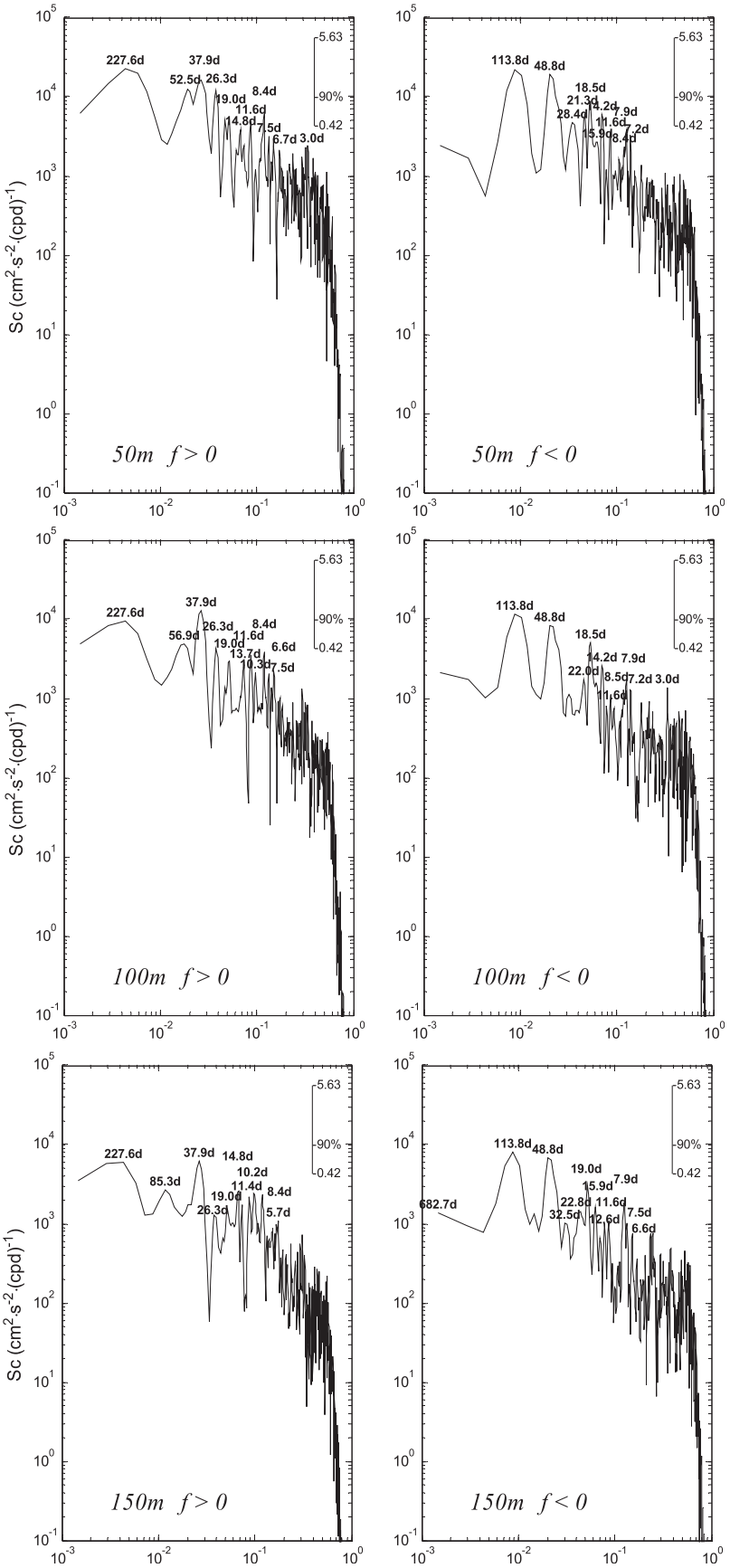

Fig. 3. Vector Rotary power spectra (Sc) from time series of current velocity vectors recorded July 7, 2009 to March 31st, 2011. Data were collected with an ADCP sensor at mooring station N2, processed with a 40 h ChebyshevⅡ low pass filter and modeled using the Welch method. The counterclockwise Rotary spectra component (f > 0) is shown left and the clockwise Rotary spectra component (f < 0) is shown right. Numbers indicate periods of the peaks in days (d) at 50 m, 100 m, 150 m, 200 m, 250 m and 296 m levels.

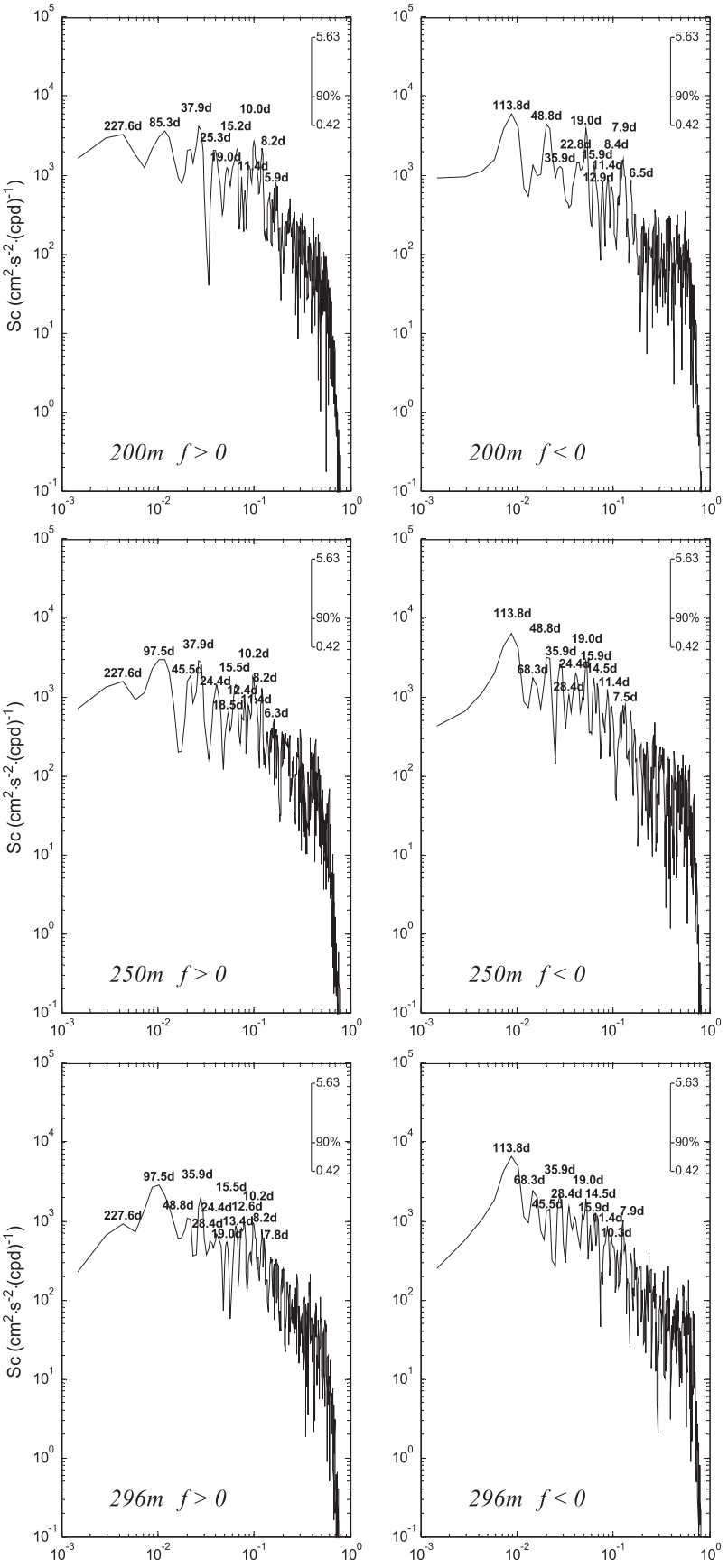

Fig. 3 (*continued*)

A very important property of the above modified wavelet transformation is that energy at any location n (corresponding to $t = 2^{-j}n$) can be derived as $E_n^j \equiv \frac{1}{\Delta t}\left[\hat{f}_n^j\right]^2 = 2^j \times \left[\hat{f}_n^j\right]^2$ (see detailed derivation in LLW07). The energy E_n^j is essentially the multiplication of the square of $\hat{f}_n^j$ and the scale factor 2^j, while the square of $\hat{f}_n^j$ is the energy associated with standard wavelet analysis. Therefore, RWPSA resolves the spectral biases in standard wavelet spectra owing to the additional scale factor (Liu et al., 2007).

4.2. Westward velocity U and northward velocity V components time series data

The dominant periods for westward velocity components U and northward V velocity components at levels of 50, 100, 150, 200, 250, and 296 m were identified using RWPSA after the following procedure (hereafter case 1). The first step was to remove the tidal signal by harmonic analysis; followed by a 48 h Chebyshev Type II digital low pass filter to remove short periods of less than 48 h; the

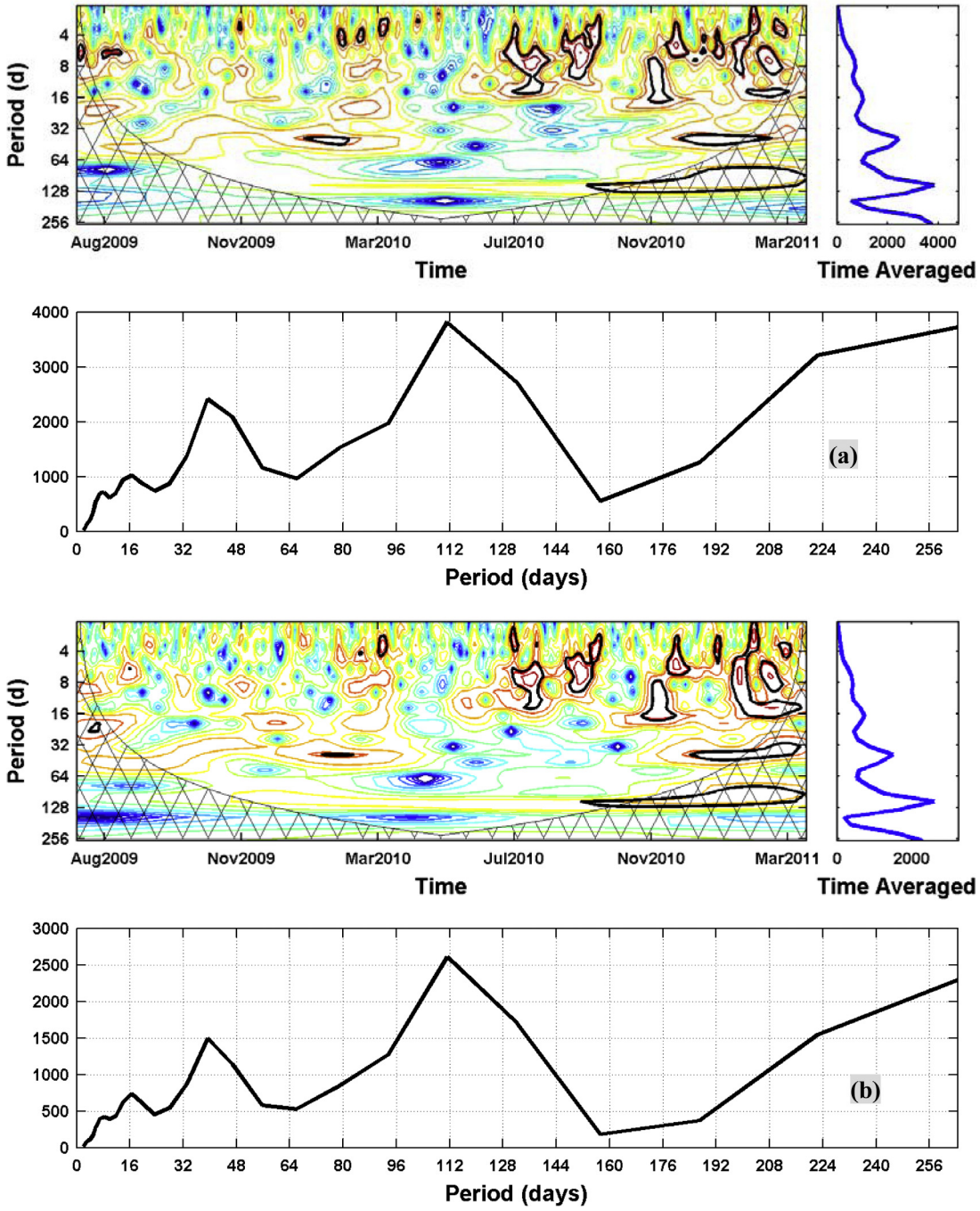

Fig. 4. (a) Top row: rectified wavelet power spectra (left column) and time-averaged rectified wavelet power spectra in base 2 logarithm (right column) for westward velocity component U time series at 50 m levels from observational current velocity at mooring station N2. Red and blue contours indicate high and low wavelet power spectrum values, respectively. The regions of greater than 95% confidence are shown with thick black contours. Cross-hatched regions indicate the "cone of influence," where edge effects become important. Bottom row: time-averaged rectified wavelet power spectra in not base 2 logarithm for western velocity component U time series at 50 m; (b) same as (a) for western velocity component U at 100 m depth.

final step was to calculate the daily mean after the low pass filtering.

4.2.1. Westward velocity component U time series data

Figs. 4–11(a) and (b) show RWPSA (top left) and associated time-averaged power spectra (bottom). The power spectra in $\log_2$ base are also shown in the top right, which has a different time unit, with time-averaged power spectra (bottom), for reference. Note that the wavelet power spectrum, included in the upper-right corner of Figs. 4–11(a) and (b) does not have a unit since the time series has been normalized (subtraction of mean and division by the standard deviation). We analyze firstly longer period variations of the Kuroshio in the LS using RWPSA for westward velocity component U time series data. Figs. 4–6 show two types of dominant periods for the westward velocity component U time series from 50 m to 296 m depth.

(1) From Figs. 4–6(a) and (b), it is seen that (1) the peak area in the period of 110–118 d occurs in most of time area with the 95% significance contours; (2) The most dominant period is 112 d, which occurs throughout the upper layer from the surface to 296 m, with the dimensionless magnitudes of strongest power spectral density for westward velocity component U time series $(\text{PSD-U})_{\max}$ to be about 3800, 2600, 1900, 1400, 1370, and 1080 at depths of 50, 100, 150, 200, 250, and 296 m, respectively. This shows that the maximum power spectral density decrease with deeper depths, i.e., the depth dependence of maximum PSD. It is worthy of note

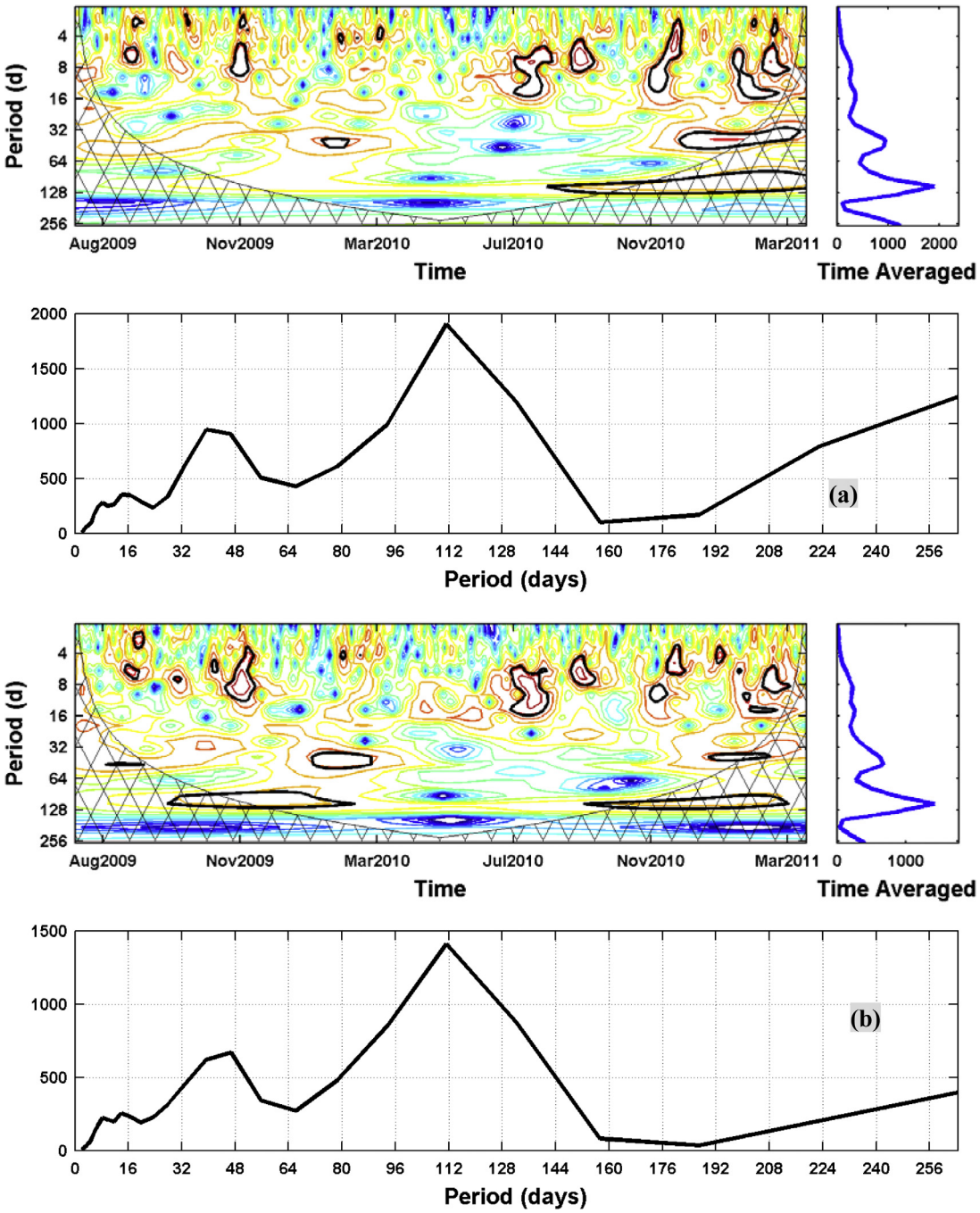

Fig. 5. Same as Fig. 4 for (a) 150 m depth; (b) 200 m depth.

that the physical unit of PSD is $(cms^{-1})^2$/cpd, however, in the wavelet power spectrum PSD does not have a unit since the time series has been normalized, as the above. In combination with analysis of vector rotary spectra discussed in Section 3 and Fig. 2, it is clear that the occurrence of the most dominant period in the upper 300 m is related to the clockwise meandering of the Kuroshio into the LS. Because the above important characteristics and the dominant period of 112 d are present at all depths, it is termed the first type of dominant period.

(2) The next most dominant periods are: (i) 8 d between 50 and 200 m depth; (ii) 16 d and 40 d between 50 and 150 m depth (the 16 d period is slightly reduced below 200 m); and (iii) 47 d between 200 and 296 m depth. In combination with analysis of vector rotary spectra in Section 3, it suggests that (1) 8 d and 16 d is related to both the clockwise and anticlockwise meandering of the Kuroshio (2) 47 d is related to the clockwise meandering of the Kuroshio. The variable depths at which these dominant periods occur suggest dependence on the vertical level. These are termed the second type of dominant period, which has quite different characteristics to the first type.

4.2.2. Northward velocity component V time series data

Figs. 7–9 show RWPSA and associated power spectrum for the northward velocity component V time series. From Figs. 7–9a)

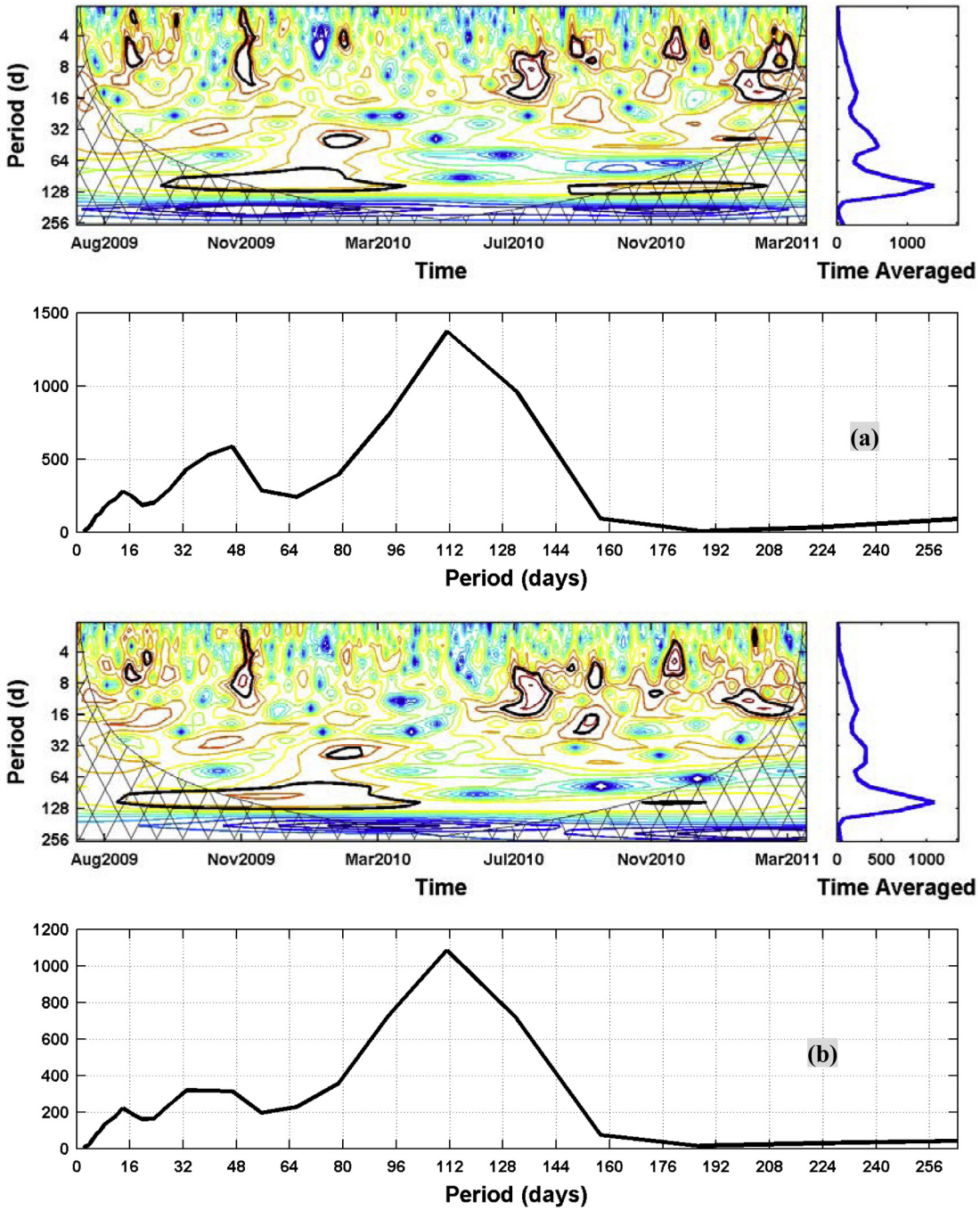

Fig. 6. Same as Fig. 4 for (a) 250 m depth; (b) 296 m depth.

and (b), it is seen that (1) the peak area in the period of 110–118 d occurs in most of time area with the 95% significance contours; (2) The most dominant period here is also 112 d, with the dimensionless magnitudes of strongest power spectral density for the northward velocity component V time series $(PSD\text{-}V)_{max}$ to be about 3550, 1400, 1250, 1250, 1220, and 1350 at depths of 50, 100, 150, 200, 250, and 296 m, respectively. This shows also that the maximum power spectral density decrease with deeper depths, i.e., the depth dependence of maximum PSD. Similar to the westward component U, the occurrence of the most dominant period 112 d in the upper 300 m is closely related to the clockwise meandering of the Kuroshio into the LS and belongs to the first type of dominant period. The next most dominant periods are more numerous in the northward component V time series: periods of 8 d and 24 d from 50 to 200 m; a period of 40 d from 100 to 250 m; periods of 66 d and about 224 d occurred at the 296 m level only. In combination with analysis of vector rotary spectra in Section 3, it suggests that (1) 8 d is related to both the clockwise and anticlockwise meandering of the Kuroshio; (2) 24 and 40 d are only related to the anticlockwise meandering of the Kuroshio. These belong to the second type of dominant period, and have the same characteristics as the western velocity U, occurring at variable depths and showing dependence on the vertical level.

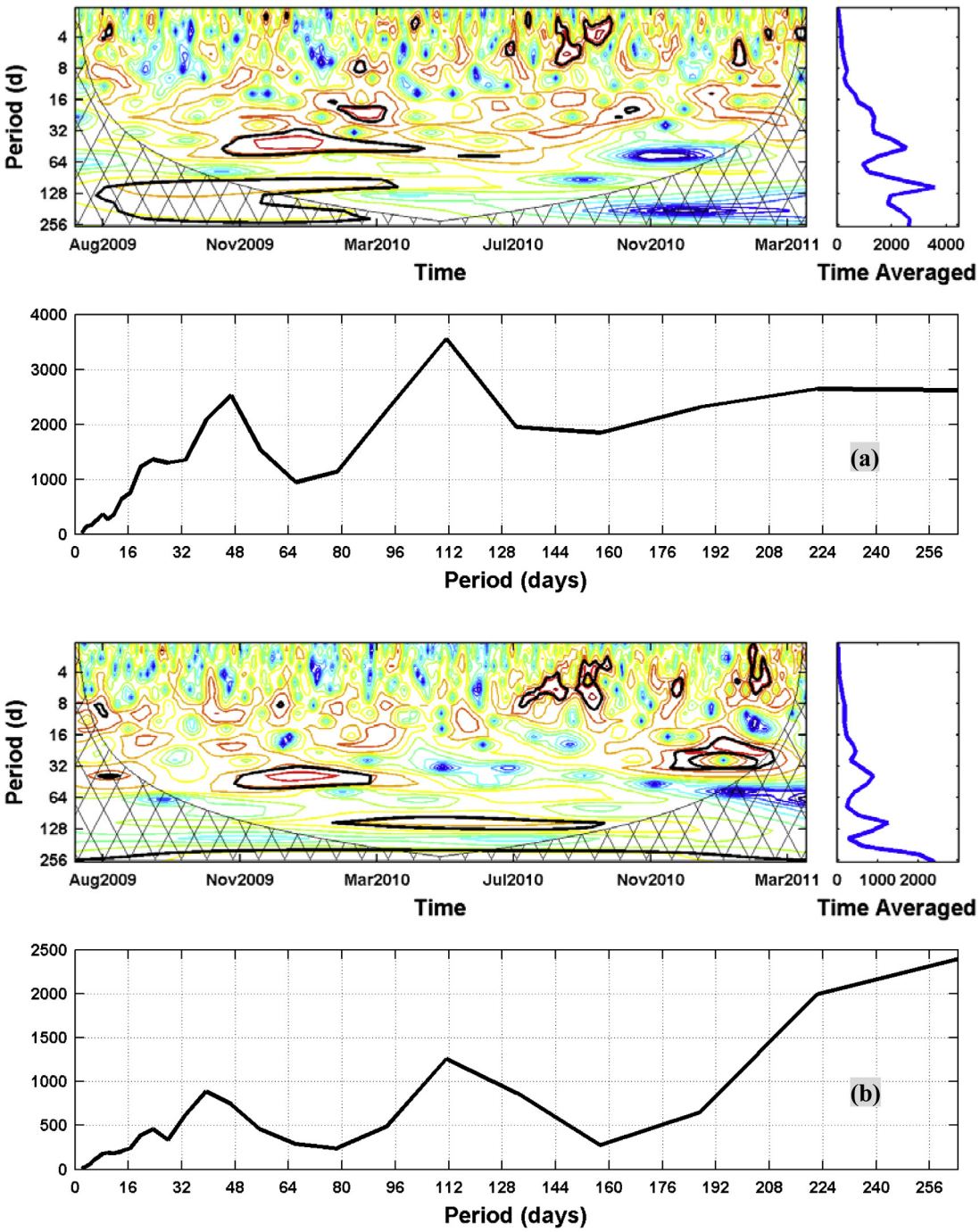

Fig. 7. Same as Fig. 4 for northern velocity component V time series at (a) 50 m depth; (b) 100 m depth.

4.3. TD pressure and temperature time series data

Here, dominant periods for the pressure and temperature time series data are further assessed using RWPSA, following the same procedure as the velocity component, i.e., case 1. Figs. 10a and 11a show the corresponding pressure and temperature time series at TD-340 m in case 1. The strongest peak still occurs at the dominant period of 112 d for both pressure and temperature time series, but the secondary periods are slightly different. Both time series have secondary periods of 223 d and 15–16 d, while the pressure time series has an additional period of 47 d.

The time series without removal of the tidal harmonic was also analyzed, so that only a 48 h Chebyshev Type II digital low pass filter was performed to remove high frequency periods less than 48 h, i.e., semi-diurnal and diurnal tidal signals (hereafter case 2). The four dominant periods in the pressure series are the fortnightly spring-neap tides (14 d), solid Earth tides (28 d), 112 d and an additional period of 186 d (Fig. 10b). However, the dimensionless magnitudes of power spectral density at 14 d is stronger than that at 112 d (Fig. 10b), which is quite differ from Fig. 11b in the temperature time series. In the temperature time series, the strongest peak still occurs at the dominant period of 112. The secondary periods are the fortnightly spring-neap tides (14 d), solid Earth tides (28 d) and 223 d (Fig. 11b).

From Figs. 4–11(a) and (b), it is clear that (1) the first type of dominant period of 112 d is present at all depths from 50 m to 365 m; (2) the second type of dominant period occurred at variable depths and showed dependence on the vertical level, which has quite different characteristics to the first type; (3) the fortnightly spring-neap tides (14 d) and solid Earth tides (28 d) only occurred

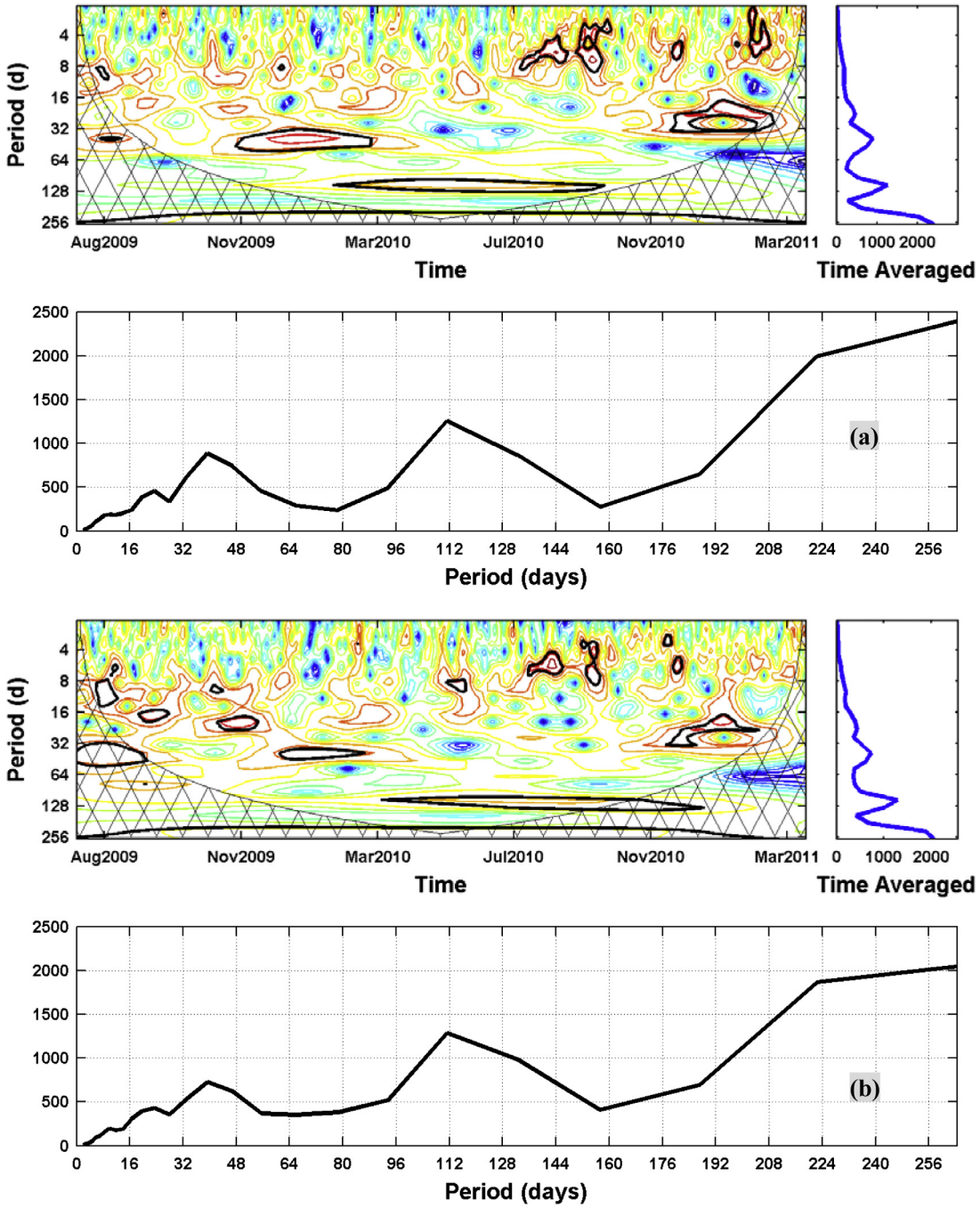

Fig. 8. Same as Fig. 4 for northern velocity component V time series at (a) 150 m depth; (b) 200 m depth.

in case 2. Especially the strongest peak at the fortnightly spring-neap tides (14 d) only occurs in case 2 of the pressure series (Fig. 10b). This is because (1) case 2 only remove high frequency periods less than 48 h, i.e., semi-diurnal and diurnal tidal signals, which quite differ from case 1 for computer procedure, (2) the characteristics of dominant tidal periods in the pressure series is differ from that in the temperature time series.

5. Discussion

5.1. Comparison between the VRS analysis and RWPSA

The dominant periods identified by VRS analysis and RWPSA are consistent. The most dominant period of 112 d identified in the RWPSA corresponds approximately to the period of 113.8 d in the VRS analysis. The periods of 8, 14, 16, and 28 d are identified in both the RWPSA and VRS data. Finally, the periods 24, 40, and 47 d in the RWPSA data corresponds approximately to the periods 23–26, 38, and 48.8 d in the VRS data. From the VRS analysis, the dominant spectral peaks have two different characteristics for rotary spectra components, i.e., both clockwise ($f < 0$) and counter-clockwise ($f > 0$) rotary spectra components, not that by RWPSA. However, following results are obtained only from RWPSA, not that by VRS analysis. They are (1) RWPSA provides two important types of dominant period. The first type has quite different characteristics to the second type. (2) The power spectral density can been determined only from RWPSA. For example, for first type of dominant period, the strongest power spectral density has a period of 112 d, and maximum power spectral density $(PSD\text{-}W)_{max}$ and $(PSD\text{-}N)_{max}$ are obtained in the upper 300 m. Furthermore, the

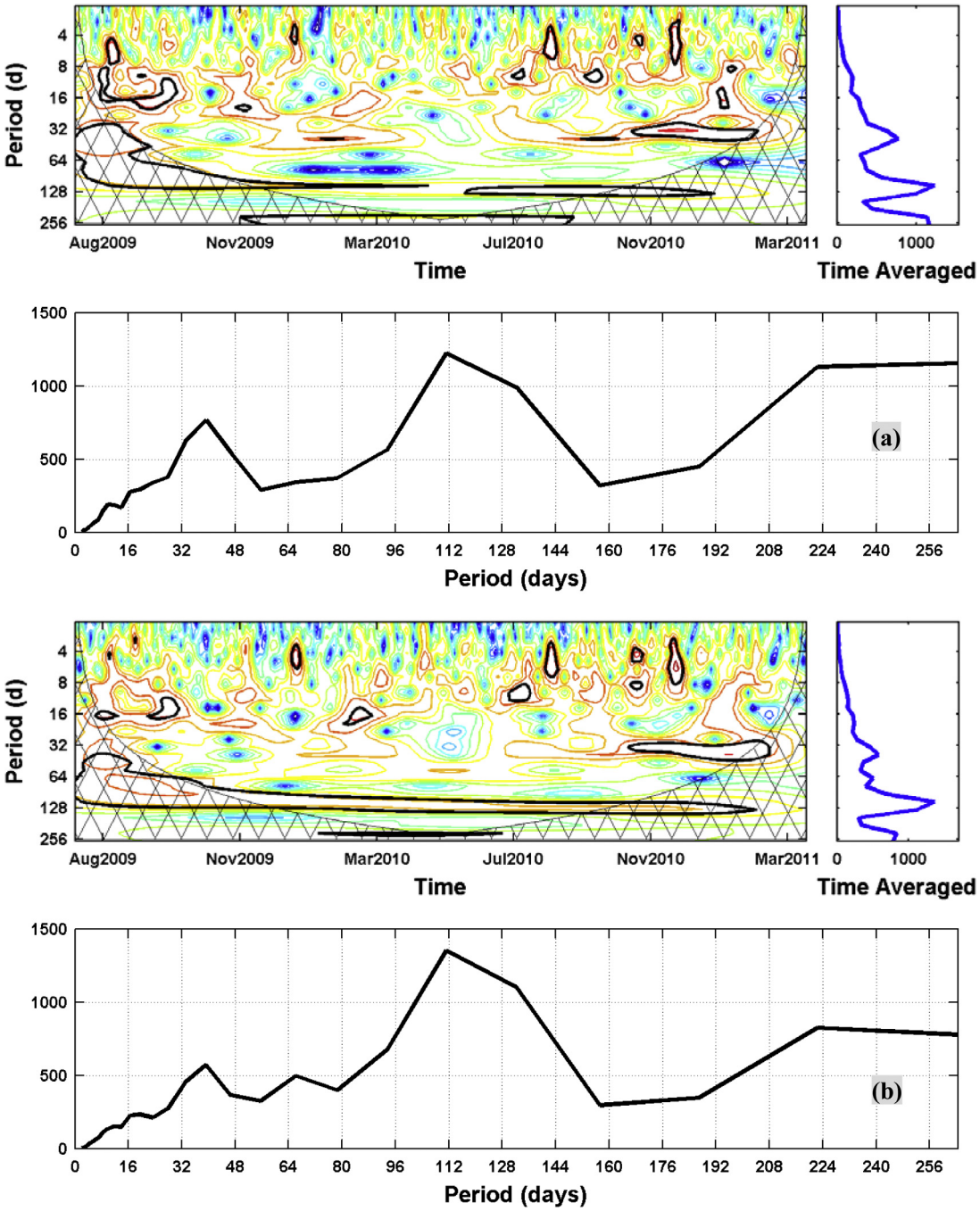

Fig. 9. Same as Fig. 4 for northern velocity component V time series at (a) 250 m depth; (b) 296 m depth.

analysis in Section 4 suggests that use of RWPSA results in a substantial improvement in the spectral estimate. This is mainly because it incorporates a physically consistent definition of energy for the wavelet power spectrum, that is the square of the transformation coefficient divided by its associated scale, as Liu et al. (2007) pointed out. Thus, dominant periods are more accurately estimated from RWPSA, while VRS analysis is limited by the lower accuracy of spectral peaks. If the RWPSA is combined with the VRS analysis, we may allow better assessment of potential causal mechanisms for the dominant spectral peaks.

5.2. Two types of dominant periods

5.2.1. Causes of the most dominant period of 112 d

Since the harmonic tidal signals and periods shorter than 48 h were removed in these results, the long period variation will be addressed here. Fig. 2 suggests that the Kuroshio intrusion into the LS is oriented northwestward, with anticyclonic and cyclonic meanders above the 300 m level. In particular, The strongest peak intensities in Figs. 4–9 confirm that the most dominant period of 112 d occurred in the upper 300 m. In combination with analysis of vector rotary spectra discussed in Section 3, it is clear that the occurrence of the most dominant period in the upper 300 m is related to the clockwise meandering of the Kuroshio into the LS. The strongest spectral peaks in the pressure and temperature time series further support the 112 d dominant period.

Which of mechanism causes the clockwise meandering of the Kuroshio into the LS? First of all, we discuss simply the mesoscale eddy near the LS. Mesoscale eddy properties in the northwestern subtropical Pacific Ocean were investigated by Yang et al. (2013). They analyzed 22,567 cyclonic eddies (CEs) and 26,365 anticyclonic eddies (AEs) detected from 19 year altimetric sea level records. Eddy occurrence frequency and kinetic energy are prevailingly high in the Subtropical Countercurrent zonal band between 19°N and 26°N and further elevated near the Luzon-Taiwan coast. They further pointed out that AEs along the Luzon-Taiwan coast were preferentially strengthened by the northward background flow.

We have made the results of statistic analysis for the cyclonic and anticyclonic eddies by the method from Nencioli et al.

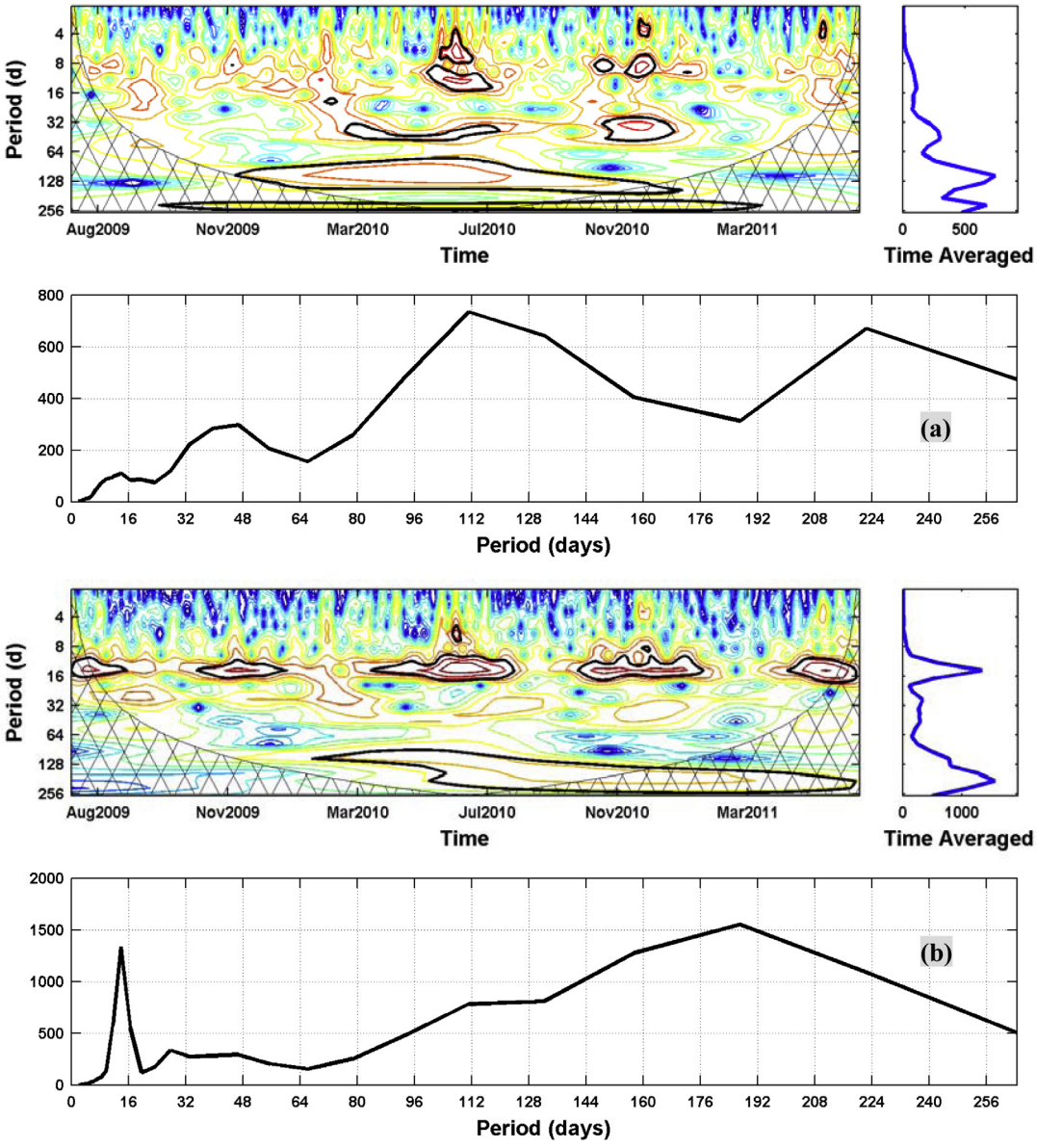

Fig. 10. Same as Fig. 4 for the pressure time series data at 340 m levels recorded by TD-340 m at mooring station N2 in (a) case 1 and (b) case 2.

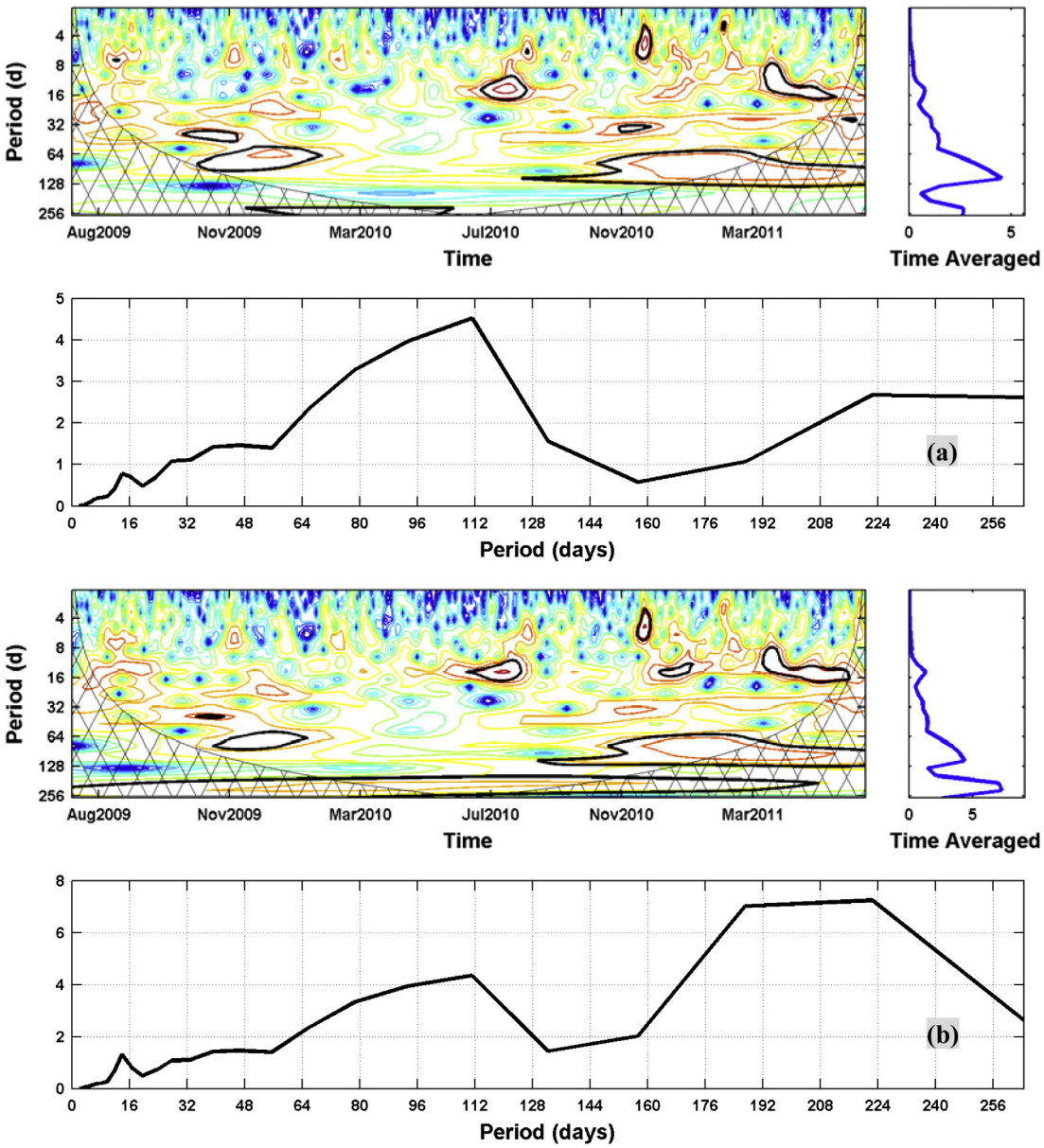

Fig. 11. Same as Fig. 4 for the temperature time series data at 340 m levels recorded by TD-340 m at mooring station N2 in (a) case 1 and (b) case 2.

(2010) in the area east of the Luzon Strait during three year altimetric sea level records from 2009 to 2011. The altimeter products were produced and distributed by Aviso (http://www.aviso.altimetry.fr/), as part of the Ssalto ground processing segment. Spatial resolution of a daily global covered data is available: 1/4°x1/4° on a cartesian grid. The first step is to search the eddies in a greater area (15°N–25°N, 122.5°E–132°E) (see Fig. 12); then the eddies are counted and their mean centers during its lifespan are limited within an area (18°N–22°N, 122.5°E–132°E); the final step was to remove the eddies whose lifespan are shorter than 3 days. From the results of statistic analysis for mesoscale eddy, their properties in an area (18°N–22°N, 122.5°E–132°E) are as follows. (1) We analyzed 118 cyclonic eddies (CEs) and 133 anticyclonic eddies (AEs) detected during three year altimetric sea level records from 2009 to 2011; (2) For maximum radius greater than 150 km, 7 CEs and 9 AEs; (3) For maximum radius greater than 100 km, 29 CEs and 38 AEs; (4) For maximum radius less than 50 km, 92 CEs and 103 AEs; (5) For maximum radius less than 50 km, 41 CEs and 36 AEs. Fig. 12 shows the westward propagating stronger anticyclonic eddy during March 10–22, 2010. On March 22, 2010, the anticy-clonic eddy is located at area east of the LS.

For the problem of mesoscale eddy propagation into the LS, the question is what role the Kuroshio plays in the interaction of eddies with the Kuroshio at the LS. Based on satellite altimeter sea level data from 1993 to 2008, Zheng et al. (2011) analyzed the interaction of nonlinear Rossby eddies with the Kuroshio at the Luzon Strait. They pointed out that before entering the LS, eddies meet the Kuroshio first. For small eddies, the Kuroshio might serve as a dynamic shield to block eddies' westward propagation. For large eddies, the Kuroshio is unable to keep itself unchanged under the forcing by a large eddy or multiple eddies. In contrast, the Kuroshio mainstream path is modified by eddies, including cutting off, meandering and branching. Especially, they gave a complete description of Kuroshio branching process in the case study in Section 5. For example, they showed that the eddy penetrating through the LS and entering into the SCS occurred simultaneously with the Kuroshio branching. Their westward propagation speed reached as high as 0.67 m s^{-1}. The conditions

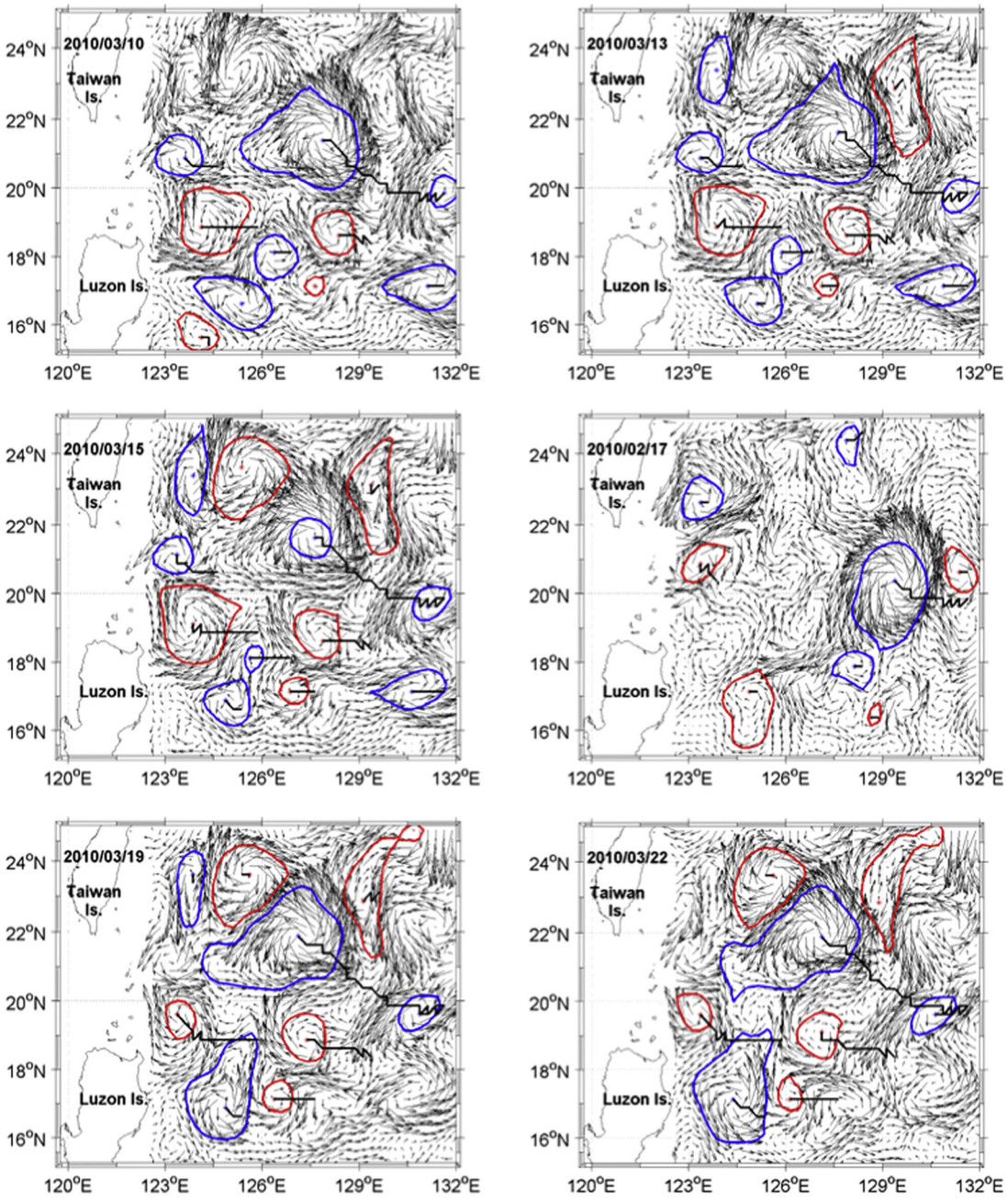

Fig. 12. The westward propagating cyclonic and anticyclonic eddies in area (15°N–25°N, 122.5°E–132°E) during March 10–22, 2010.

for branching occurrence were: the strong anticy-clonic eddy east of the LS (central dynamic height 45–50 cm higher than the local mean) forces the Kuroshio meander to develop to a westward warm water tongue, and so on. According to analysis of Zheng et al. (2011), it is seen that the clockwise meandering of the Kuroshio intrusion into the LS is caused by the westward propagating stronger anticy-clonic eddy due to the interaction of nonlinear Rossby eddies with the Kuroshio.

Therefore, it is easy to reach the conclusion that the dominant period of 112 d is strongly related to clockwise meandering of the Kuroshio into the LS, which is caused by westward propagating stronger anticyclonic eddies (see Fig. 12) from the interior ocean due to the interaction of nonlinear Rossby eddies with the Kuroshio. This conclusion is basically consistent with the results by Yang et al., 1999, 2001; Zhang et al., 2001; Lee et al., 2001, namely, on the 100-day timescale occurred in the East Taiwan Channel at 24.5°N, the Kuroshio transport entering the East China Sea is strongly related to meandering of the Kuroshio, which in turn is caused by westward propagating anticyclonic eddies from the interior ocean.

5.2.2. Second type of dominant periods

Second type of dominant period have three cases as follows. (1) 8 d and 16 d are related to both the clockwise and anticlockwise meandering of the Kuroshio (2) 47 d is related to the clockwise meandering of the Kuroshio. (2) 24 and 40 d are only related to the anticlockwise meandering of the Kuroshio. It worthy of note that the above next dominant periods 40 d and 16 days corresponds approximately to the dominant period of 40 days and 18 days occurred in the East Taiwan Channel at 24.5°N (see Zhang et al., 2001; Lee et al., 2001).

5.3. Dominant tidal periods of more than 48 h

Figs. 10b and 11b confirm the dominant period of 14 d is the fortnightly spring-neap tidal period that has been reported in previous studies (Yuan et al., 2009b; Liao et al., 2012), and the next most dominant period of 28 d (time scale of two weeks) is the solid Earth tide.

6. Conclusions

Observations of ADCP current velocity (50–300 m), and pressure and temperature time series data recorded by two TDs (340 m and 365 m), at mooring station N2 provides strong evidence of longer period variation of the Kuroshio intrusion into the LS using the VRS and RWPSA. The VRS analysis can determine two different characteristics for rotary spectra components, i.e., both clockwise ($f < 0$) and counterclockwise ($f > 0$) rotary spectra components for the dominant spectral peaks. However, RWPSA provides better estimates of dominant periods than VRS analysis, and two important types of dominant period have been determined.

(1) First type of dominant period. The strongest power spectral density has a period of 112 d, is observed in the upper 300 m. The dimensionless magnitudes of maximum power spectral density for westward velocity component U time series $(PSD\text{-}U)_{max}$ to be about 3800, 2600, 1900, 1400, 1370, and 1080 at depths of 50, 100, 150, 200, 250, and 296 m, respectively, and the dimensionless magnitudes of maximum power spectral density for the northward velocity component V time series $(PSD\text{-}V)_{max}$ to be about 3550, 1400, 1250, 1250, 1220, and 1350 at depths of 50, 100, 150, 200, 250, and 296 m, respectively. This shows that the maximum power spectral density decrease with deeper depths, i.e., the depth dependence of maximum PSD. In combination with analysis of vector rotary spectra and mechanism analysis, it is clear that the occurrence of the most dominant period of 112 d in the upper 300 m is related to the clockwise meandering of the Kuroshio into the LS, which is caused by westward propagating stronger anticyclonic eddies from the interior ocean due to the interaction of nonlinear Rossby eddies with the Kuroshio. This conclusion is basically consistent with the results on the 100-day timescale occurred in the East Taiwan Channel at 24.5°N by Yang et al., 1999, 2001; Zhang et al., 2001; Lee et al., 2001.

(2) Second type of dominant period. The next dominant periods of 8 d and 16 d are related to both the clockwise and anticlockwise meandering of the Kuroshio; 47 d is related to the clockwise meandering of the Kuroshio; 24 d and 40 d are only related to the anticlockwise meandering of the Kuroshio. The above next dominant periods 40 d and 16 days corresponds approximately to the dominant period of 40 days and 18 days occurred in the East Taiwan Channel at 24.5°N by Zhang et al. (2001) and Lee et al.(2001).

Finally, the dominant period of 14 d is the fortnightly spring-neap tidal period, and the next dominant period of 28 d (time scale of two weeks) is the solid Earth tide.

Acknowledgments

We gratefully acknowledge Drs. Yonggang Liu and X. San Liang for his very valuable suggestions and discussion, especially, Dr. Yonggang Liu provided computational program for our calculation of the rectified wavelet power spectra. This work was supported by the National Basic Research Program of China (No. 2014CB441501, 2007 CB816003), the project of the National Natural Science Foundation of China (No. 41576001, 41406021, 41621064), the Scientific Research Fund of SIO (JT1604 and JG1621), the National Programme on Global Change and Air-Sea Interaction (GASI-IPOVAI-01-02), the Project of State Key Laboratory of Satellite Ocean Environment Dynamics, SIO (grand SOEDZZ1507), the National Programme on Global Change and Air-Sea Interaction (grand GASI-IPOVAI-04), the International Cooperative Project of the Ministry of Science and Technology of China (No. 2006DFB21630) and the National key research and development program (No. 2016YFC0304105). We wish to thank their supports. We also wish to thank the crew and participants of the R/V Dong Fang Hong-2 and the R/V Zhongda-31 for their supports and cooperation.

References

Cai, S.Q., Liu, H.L., Li, W., Long, X.M., 2005. Application of LICOM to the numerical study of the water exchange between the South China Sea and its adjacent oceans. Acta Oceanol. Sin. 24 (4), 10–19.
Cai, S.Q., Zheng, S., He, Y.H., 2012. Vorticity budget study on the seasonal upper circulation in the northern South China Sea from altimetry data and a numerical model. J. Ocean Univ. Chin. 11 (4), 455–464.
Chen, C.-T.A., Jan, S., Huang, T.-H., Tseng, Y.-H., 2010. Spring of no Kuroshio intrusion in the southern Taiwan Strait. J. Geophys. Res. 115, C08011.
Chen, S.J., Ma, J.R., 1991. The Methods of the Oceanic Data Processing and Analysis and Their Application. China Ocean Press, Beijing (in Chinese).
Du, T., Tseng, Y.H., Yan, X.H., 2008. The impacts of tidal currents and Kuroshio intrusion on the generation of nonlinear internal waves in Luzon Strait. J. Geophys. Res. – Ocean 113, C08015.
Fang, G.H., Wei, Z., Choi, B.H., Wang, K., Fang, Y., Li, W., 2003. Interbasin freshwater, heat and salt transport through the boundaries of the East and South China Seas from a variable-grid global ocean circulation model. Sci. Chin. (Ser. D), 46(2), 149–161.
Fang, G.H., Wang, Y.G., Wei, Z.X., Fang, Y., Qiao, F.L., Hu, X.M., 2009. Interocean circulation and heat and freshwater budgets of the South China Sea based on a numerical model. Dynam. Atmos. Oceans 47, 55–72.
Lee, T.N., Johns, W.E., Liu, C.-T., Zhang, D.X., Zantopp, R., Yang, Y., 2001. Mean transport and seasonal cycle of the Kuroshio east of Taiwan with comparison to the Florida Current. J. Geophys. Res. 106(C10), 22143–22158 (October 15).
Liang, X.S., Anderson, D.G.M., 2007. Multiscale window transform. SIAM J. Multiscale Model. Simul. 6, 437–467.
Liao, G.H., Yuan, Y.C., Kaneko, A., Yang, C.H., Chen, H., Taniguchi, N., Gohda, N., Minamidate, M., 2011. Analysis of internal tidal characteristics in the layer above 450 m from acoustic Doppler current profiler observations in the Luzon Strait. Sci. Chin. (Ser. D) 54 (7), 1078–1094. http://dx.doi.org/10.1007/s11430-010-4102-0.
Liao, G.H., Yuan, Y.C., Yang, C.H., Chen, H., Wang, H.Q., Huang, W.G., 2012. Current observations of internal tides and parametric subharmonic instability in the Luzon Strait. Atmosphere-Ocean 50(suppl.), 59–76.
Liu, Y.G., Weisberg, R.H., Yuan, Y.C., 2008. Patterns of upper layer circulation variability in the South China Sea from satellite altimetry using the self organizing map. Acta Oceanol. Sin. 27 (Suppl.), 129–144.
Liu, Y.G., Liang, X.S., Weisberg, R.H., 2007. Rectification of the bias in the wavelet power spectrum. J. Atmos. Ocean. Technol. 24 (12), 2093–2102.
Metzger, E.J., Hurlburt, H.E., 1996. Coupled dynamics of the South China Sea, the Sulu Sea, and the Pacific Ocean. J. Geophys. Res. 101, 12331–12352.
Meyer, Y., 1992. Wavelets and Operators. Cambridge University Press, p. 223.
Nan, F., Xue, H., Yu, F., 2015. Kuroshio intrusion into the South China Sea: a review. Progr. Oceangr. 137, 314–333.
Nencioli, F., Dong, C., Dickey, T., Washburn, L., McWilliams, J.C., 2010. A vector geometry-based eddy detection algorithm and its application to a high-resolution numerical model product and high-frequency radar surface velocities in the Southern California bight. J. Atmos. Ocean. Technol. 27, 564–579.
Park, J.-H., Farmer, D., 2013. Effects of Kuroshio intrusions on nonlinear internal waves in the South China Sea during winter. J. Geophys. Res. Oceans 118, 7081–7094.
Qu, T., Kim, Y.Y., Yaremchuk, M., Tozuka, T., Ishida, A., Yamagata, T., 2004. Can Luzon Strait Transport play a role in conveying the impact of ENSO to the South China Sea? J. Clim. 17, 3644–3657.
Qu, T., 2000. Upper layer circulation in the South China Sea. J. Phys. Oceanogr. 30, 1450–1460.
Qu, T., Song, Y.T., Yamagata, T., 2009. An introduction to the South China Sea throughflow: its dynamics, variability, and application for climate. Dyn. Atmos. Ocean. 47, 3–14.
Torrence, C., Compo, G.P., 1998. A practical guide to wavelet analysis. Bull. Am. Meteor. Soc. 79, 61–78.

Tseng, Y.H., Shen, M.L., Jan, S., Dietrich, D.E., Chiang, C.P., 2012. Validation of the Kuroshio current system in the dual-domain Pacific Ocean model framework. Prog. Oceanogr. 105, 102–124.

Tzeng, W.-N., Tseng, Y.-H., Han, Y.-S., Hsu, C.-C., Chang, C.-W., Di Lorenzo, E., Hsieh, C.-H., 2012. Evaluation of multi-scale climate effects on annual recruitment levels of the Japanese Eel, Anguilla japonica, to Taiwan. PLoS ONE 7, e30805.

Welch, P.D., 1967. The use of fast Fourier transform for the estimation of power spectra: a method based on time averaging over short, modified periodograms. IEEE Trans. Audio Electroacoust. AU-15, 70–73.

Yang, G., Wang, F., Li, Y.L., Lin, P.F., 2013. Mesoscale eddies in the northwesternsubtropical Pacific Ocean: statistical characteristics and three-dimensional structures. J. Geophys. Res.: Oceans 118, 1906–1925. http://dx.doi.org/10.1002/jgrc.20164.

Yang, Y., Liu, C.-T., Hu, J.-H., Koga, M., 1999. Taiwan current (Kuroshio) and impinging eddies. J. Oceanogr. 55, 609–617.

Yang, Y., Liu, C.-T., Lee, T.N., Johns, W.E., Li, H.W., Koga, M., 2001. Sea surface slope as the estimator of the Kuroshio volume transport east of Taiwan. Geophys. Res. Lett. 28, 2461–2464.

Yuan, Y.C., Liao, G.H., Xu, X.H., 2007. Three dimensional diagnostic modeling study of the South China Sea circulation before onset of summer monsoon in 1998. J. Ocean. 63, 77–100.

Yuan, Y.C., Liao, G.H., Guan, W.B., Wang, H.Q., Lou, R.Y., Chen, H., 2008. The circulation in the upper and middle layers of the Luzon Strait during spring 2002. J. Geophys. Res. 113, C06004. http://dx.doi.org/10.1029/2007JC004546, 1–18.

Yuan, Y.C., Liao, G.H., Yang, C.H., 2009a. A diagnostic calculation of the circulation in the upper and middle layers of the Luzon Strait and the northern South China Sea during March 1992. Dyn. Atmos. Ocean. 47, 86–113.

Yuan, Y.C., Liao, G.H, Wang, H.Q., Chen, R.Y.H., (2009b. Variability of the currents in the Luzon Strait during spring of 2002 obtained from observations and satellite geostrophic currents and spectral analyses. Sci. Chin. (Ser. D) 52(4), 519–531.

Yuan, Y.C., Liao, G.H., Kaneko, A., Yang, C.H., Zhu, X.-H., Chen, H., Gohda, N., Taniguchi, N., Minamidate, M., 2012a. Currents in the Luzon Strait obtained from moored ADCP observations and a diagnostic calculation of circulation in spring 2008. Dyn. Atmos. Ocean. 58, 20–43.

Yuan, Y.C., Liao, G.H., Yang, C.H., Liu, Z.-H., Chen, H., 2012b. Currents in the Luzon Strait evidenced by CTD and Argo observations and a diagnostic model in October 2008. Atmos. Ocean 50 (Suppl. 1), 27–39.

Yuan, Y.C., Liao, G.H., Yang, C.H., Liu, Z.H., Chen, H., Wang, Z.-G., 2014a. Summer Kuroshio Intrusion through the Luzon Strait confirmed from observations and a diagnostic model in summer 2009. Prog. Oceanogr. 121, 44–59.

Yuan, Y.C., Tseng, Y.-H., Yang, C.H., Liao, G.H., Chow, C.H., Liu, Z.H., Zhu, X.-H., Chen, H., 2014b. Variation in the Kuroshio intrusion: modeling and interpretation of observations collected around the Luzon Strait from July, 2009 to March, 2011. J Geophys. Res: Oceans 119, 3447–3463. http://dx.doi.org/10.1002/2013JC009776.

Yuan, Y.C., Zhu, X.-H., Zhou, F., 2015. Progress of studies in China from July 2010 to May 2015 on the influence of the Kuroshio on neighboring Chinese Seas and the Ryukyu Current. Acta Oceanol. Sin. 34 (12), 1–10.

Zhang, D., Johns, W.E., Lee, T.N., Liu, C.-T., Zantopp, R., 2001. The Kuroshio east of Taiwan: modes of variability and relationship to interior meso-scale eddies. J. Phys. Oceanogr. 31, 1054–1074.

Zheng, Q.N., Tai, C.-K., Hu, J.Y., Lin, H.Y., Zhang, R.-H., Su, F.-C., Yang, X.F., 2011. Satellite altimeter observations of nonlinear Rossby eddy–Kuroshio interaction at the Luzon Strait. J. Oceanogr. 67, 365–376. http://dx.doi.org/10.1007/s10872-011-0035-2.